Design of Miniaturized On-Chip Bandpass Filters Using Inverting-Coupled Inductors in (Bi)-CMOS Technology

He Zhu, *Member*, *IEEE*, Xi Zhu, *Member*, *IEEE*, Yang Yang, *Senior Member*, *IEEE*, and Yichuang Sun, *Senior Member, IEEE*

***Abstract*— In this work, a new type of miniaturized on-chip resonator using coupled-inductor structure is presented. The impact on resonances of the structure due to the use of non-inverting- and inverting-coupled configuration is extensively investigated. It has been found that using the inverting-coupled structure, a stronger resonance can be generated, which is ideally suitable for device miniaturization. To fully understand the working mechanism of the resonator and use it effectively for bandpass filter (BPF) design, simplified *LC* equivalent-circuit models and detailed theoretical analysis are provided. To further demonstrate the proposed concept is useful in practice, not only a 1st-order BPF, but also another two 2nd-order BPFs are designed and fabricated in a standard 0.13-μm (Bi)-CMOS technology. All of them are designed to have a centre frequency around 15 GHz. Their physical dimensions are 0.13 × 0.25 mm², 0.26 × 0.25 mm², 0.24 × 0.22 mm², respectively. Good agreements between simulation and measurement have been obtained, which verify that the presented design approach is suitable for miniaturized on-chip passive design.**

***Index Terms*— Bandpass filters, inductively coupled resonator, inverting coupling, non-inverting coupling, on-chip resonator.**

I. Introduction

Radio-frequency (RF) on-chip filter is a building block that can be found in many RF transceivers. One of the common design issues related to such filters is how to minimize their footprint. This is mainly due to the fact that passive components, such as spiral inductor (IND) and transmission line (TL), are inherently bulky and thus take a fairly large die area. To solve this issue without adversely affecting other performance, one of the possible techniques is to use active inductors to replace the passive ones, which have been extensively studied in the literature [1]-[2]. However, the performance of active inductors may be severely deteriorated, while the operation frequency goes above 10 GHz. Thus, research on miniaturized on-chip passive components design to support microwave and millimetre-wave technologies is emerging [3]-[8]. Furthermore, another motivation behind device miniaturization is to reduce insertion loss of passive component. For operation frequency beyond 10 GHz, one of the major sources that increases insertion loss of passive component, especially for TLs and INDs, is the so-called ohmic loss, which is related to the overall length of components. If the overall length of TL or IND can be effectively reduced, the insertion loss of them could also be reduced. Several prior works have been presented in the literature for both silicon and III/V technologies [9]-[26]. The most classical method is to fold metal strip lines so that die area can be used more effectively [9]-[13]. One of the typical examples for this method is to use 3-D inductors for amplifier design [10]-[11]. However, simply folding a metal strip does not necessarily help to reduce its overall length. As a result, the insertion loss of such metal strip is unlikely to be reduced. To effectively reduce the insertion loss of a passive component, some other approaches have also been explored, such as slow-wave structure and co-planer waveguide [14]-[20]. However, a slow-wave structure is adopted for a design, the footprint of a passive component operating below 60 GHz is still fairly large. To solve this issue, a hybrid approach that utilizes capacitive-loaded TLs or INDs has been extensively used in [21]-[26] Since metal-insulator-metal (MIM) layer is provided for the most RF-CMOS process and MIM capacitor can be implemented in a very compact way, a combination of using a relatively large capacitance with a small inductance to obtain the required resonant frequency is desirable.

In this paper, an interesting design approach is presented for miniaturized passive device implementation, especially for bandpass filters (BPFs). Two classical coupling structures, namely inverting and non-inverting coupling, are investigated. As will be shown, the inverting-coupled structure is very well suitable for BPF design with a reduced size, several BPF prototypes are developed with compact size and excellent performance. Thorough theoretical analysis is given to explore the insight characteristics of the presented approach and provide a guidance to design BPFs based on this concept. To prove the approach is feasible in practice, three BPFs are implemented and fabricated in a standard 0.13-μm (Bi)-CMOS technology and good agreements between the EM simulated and measured results are achieved.

Manuscript received XXX. This research is supported by the Australian Research Council DE160101032.

H. Zhu, X. Zhu and Y. Yang are with the School of Electrical and Data Engineering, Global Big Data Technology Centre (GBDTC), University of Technology Sydney, Ultimo, NSW 2007, Australia. Email: he.zhu@uts.edu.au; xi.zhu@uts.edu.au and yang.yang-1@uts.edu.au.

Y. Sun is with the School of Engineering and Computer Science, University of Hertfordshire, Hatfield AL10 9AB, U.K. E-mail: y.sun@herts.ac.uk.

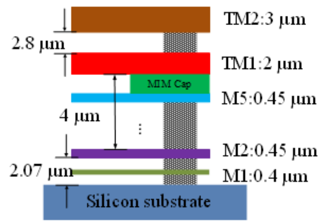

Fig. 1. Metal stack-up of the selected 0.13-μm (Bi)-CMOS technology.

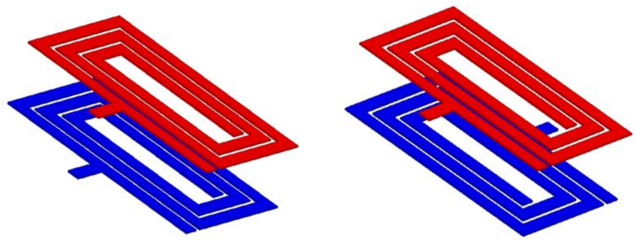

(a) (b)

Fig. 2. Two types of resonators using coupled inductors: (a) non-inverting coupled type; (b) inverting coupled type.

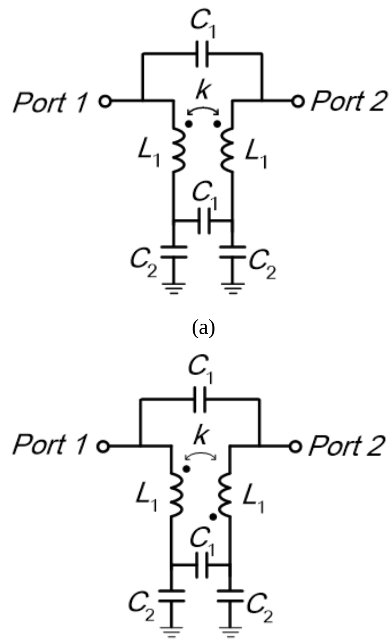

(a)

(b)

Fig. 3. Simplified *LC*-equivalent circuit models for the resonators in Fig. 2: (a) with non-inverting coupled one; (b) with inverting coupled one.

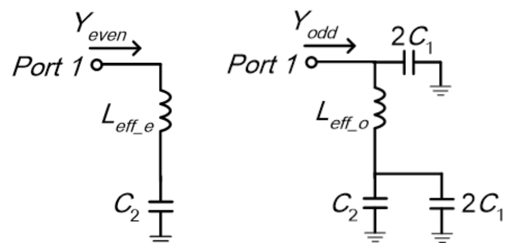

(a) (b)

Fig. 4. Even- and odd-mode analysis of the *LC*-equivalent circuit: (a) even-mode, (b) odd-mode.

The rest of this paper is organized as follows. In Section II, the inverting and non-inverting coupled structures are compared and discussed in terms of resonant poles and transmission zeros. In Section III, how to use the coupled structures for BPF design is described and design of a 1st- and 2nd-order BPFs are given as examples. To further improve out-of-band suppression for the designed BPFs, a modified resonator and its application for BPF is further explored in Section IV. The measurement results are presented in Section V and the conclusion is finally drawn in Section VI.

II. Design of Miniaturized Resonator Using Coupled-Inductor Structure

A. Overview of the Resonators Design with Different Coupling Structures

The back-end-of-line (BEOL) information is shown in Fig. 1. A standard 0.13-μm (Bi)-CMOS SiGe technology is used in the design, which provides not only high-performance transistors (with f_t of 200 GHz), but also 7 metal layers (TM1, TM2 and M1 to M5) with aluminium as the thick top two metal layers (TM1 and TM2). The additional MIM layer is placed between the sixth and fifth layers (TM1 and M5). In addition, the height of the silicon substrate is 200 μm. The dielectric constant of SiO_2 is 4.1 and the loss tangent is 0.01. In this work, two types of self-coupled resonators based on non-inverting and inverting coupling types will be discussed.

In this section, both of non-inverting and inverting-coupled resonators are theoretically analysed. Both two resonators are built on the TM1 and TM2 layers. To understand the difference between two coupling structures, 3-D views of them are provided in Fig. 2. As can be seen, each structure consists of two spiral inductors, which are identical in terms of length and width. The difference between them is how the two spiral inductors are coupled with each other. As shown in Fig. 2(a), both the upper and lower spirals are implemented in a clock -wise rotating pattern, which is called non-inverting coupled structure. Unlike this structure, as illustrated in Fig. 2(b), the lower spiral is implemented in an anti-clockwise rotating pattern. It means that the lower spiral inductor is placed in an opposite orientation of the upper one, which is known as inverting-coupled structure. Using the inverting-coupled structure, a strong inductive coupling, also known as magnetic coupling, will occur between two spirals, which makes the structure operating as a resonator.

To further illustrate the insight of this structure, more investigation is given. It will be found that with the same dimensions, the inverting-coupled structure can produce a resonant mode at a relatively lower frequency than the non-inverting-coupled one. This means that to produce a resonance at certain frequency, the inverting-coupled resonator will occupy smaller size. As will be shown in the later sections, a series of BPFs will be designed and implemented using the inverting-coupled structure for miniaturized designs. To investigate the properties of the presented resonators, further analysis and discussions will be introduced in the following sub-sections.

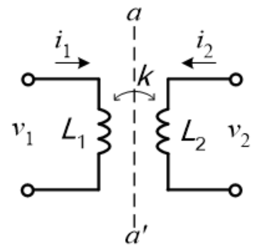

Fig. 5. A two-port network comprising two inductors including mutual coupling.

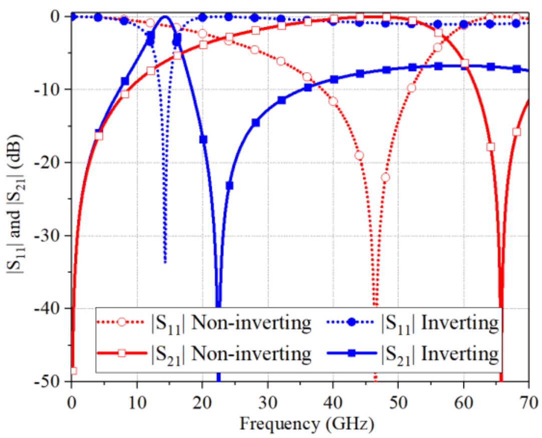

Fig. 6. Calculated S-parameters of two filters using inverting- and non-inverting- coupled structures. Related parameter values are: L_1 = 1000 pH, C_1 = 30 fF, C_2 = 10 fF, and k = -0.8 (inverting coupling) and 0.8 (non-inverting coupling).

B. Analysis of the Resonators

The above-mentioned resonators can be modelled using simplified LC-equivalent circuits, which consist of lumped inductors and capacitors. In the analysis, since the resonator is regarded as lossless, no resistors are considered in the equivalent circuits. Corresponding to Fig. 2, the LC-equivalent circuits of two resonators are shown in Fig. 3, where Fig. 3(a) shows the equivalent circuit of the non-inverting-coupled resonator, while Fig. 3(b) shows the inverting-coupled one. Both two circuit models are composed of two inductors L_1 with inductive mutual coupling M, two mutual capacitances C_1 and two grounded capacitors C_2. The capacitance C_1 denotes the electrical coupling that exists between two metal lines. C_2 is the effective grounded capacitor existing between the metal lines and the ground. Regardless the type of the resonators, both of them can be analysed using even- and odd-mode analysis method. The mutual coupling between two coupled inductors can be evaluated using a coupling coefficient k, which is $k = M/L_1$ and M represents the mutual inductance. For the case of non-inverting coupled structure, there is $0 < k < 1$; while for the case of inverting coupled one, there is $-1 < k < 0$.

The resonator can be bisected into two parts along the symmetric line: even-mode circuit and odd-mode circuit. For the even-mode circuit, the symmetric line can be regarded as a perfect magnetic conductor (PMC), and its equivalent circuit is shown in Fig. 4(a). It is a series circuit of an inductor and a capacitor. Due to the existence of mutual coupling M, the inductance in the even-mode circuit is denoted as L_{eff_e}.

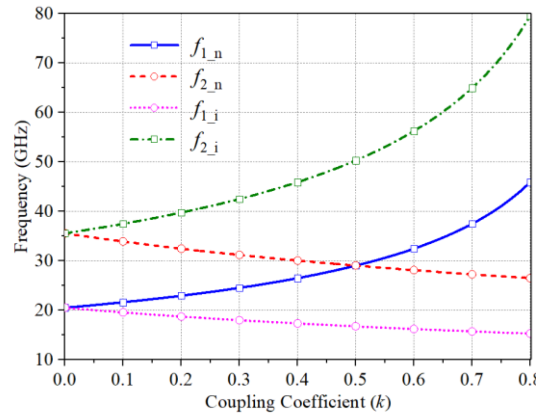

Fig. 7. Resonant mode distribution of f_{1_n}, f_{2_n}, f_{1_i} and f_{2_i} against k. Related parameter values are: L_1 = 1000 pH, C_1 = 20 fF, C_2 = 20 fF.

Therefore, the input admittance of the even-mode circuit can be expressed as:

$$Y_{even} = \frac{j \cdot \omega C_2}{1 - \omega^2 L_{eff\_e} \cdot C_2} \tag{1}$$

For the odd-mode circuit, the symmetric line can be regarded as a perfect electric conductor (PEC), and its equivalent circuit is shown in Fig. 4(b). It is composed of grounded capacitors and a series circuit of an inductor and two paralleled capacitors. Similar to the even-mode case, due to the existence of mutual coupling M, the inductance in the odd-mode circuit can be regarded as L_{eff_o}. Therefore, the input admittance of the odd-mode circuit can be expressed as:

$$Y_{odd} = \frac{j \cdot \omega (2C_1 + C_2)}{1 - \omega^2 L_{eff\_o} \cdot (2C_1 + C_2)} + j \cdot 2\omega C_1 \tag{2}$$

To determine the value of input admittance Y_{even} and Y_{odd}, the effective inductances of L_{eff_e} and L_{eff_o} must be solved. Fig. 4 displays a two-port network comprising of only two inductors with mutual inductive coupling M, which is equal to $k\sqrt{L_1 L_2}$. Assuming that $L_1 = L_2 = L$, the value of M is ranged between 0 and L. The voltage and current distribution is also marked in Fig. 4. For any inductor L itself without mutual coupling, there is $v_1 = i_1 \cdot X_l = i_1 \cdot j\omega L$, so

$$L = \frac{v_1}{j\omega \cdot i_1} \tag{3}$$

When the mutual coupling M is considered, the effective inductance is:

$$L_{eff} = \frac{v_1}{j\omega \cdot i_1} = \frac{j\omega L \cdot i_1 + j\omega M \cdot i_2}{j\omega \cdot i_1} = L + M\frac{i_2}{i_1} \tag{4}$$

For the even-mode circuit, the symmetric line $a - a'$ is regarded as a PMC. According to the mirror rule, the image current along the PMC has the same direction and magnitude of the original one; hence, $i_2 = i_1$. Therefore, the effective inductance L_{eff_e} in the even-mode circuit is

$$L_{eff_e} = L + M \tag{5}$$

For the odd-mode circuit, the symmetric line $a - a'$ is regarded as a PEC. According to the mirror rule, the image

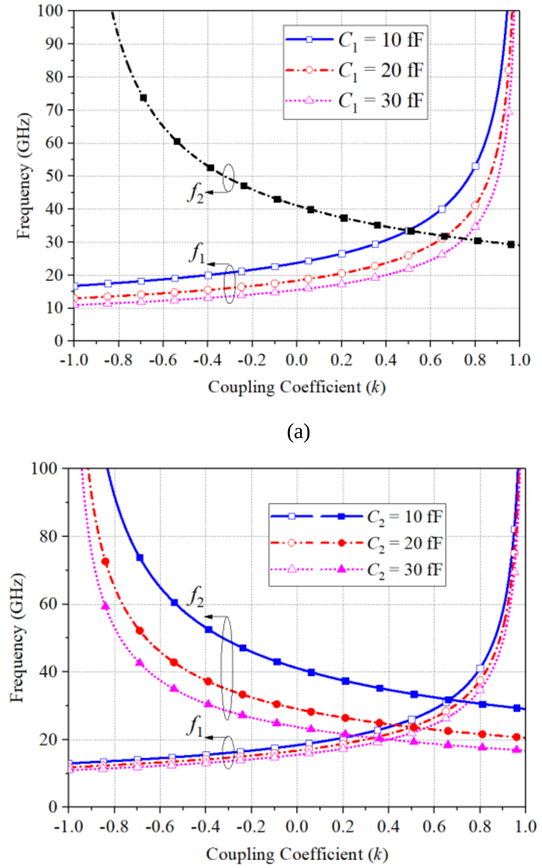

(a)

(b)

Fig. 8. The values of resonant poles against coupling coefficient k when different values of C_1 and C_2 are chosen: (a) C_1 is varied from 10 to 30 fF, (b) C_2 is varied from 10 to 30 fF.

current along the PEC has the same magnitude and opposite direction compared with the original one; hence, in this case $i_2 = -i_1$, and thus the odd-mode effective inductance L_{eff_o} is

$$L_{eff\_o} = L - M \tag{6}$$

From (5) and (6), it is obviously seen that the value of L_{eff_e} will increase with M and its value is ranged from L and $2L$; while L_{eff_o} will decrease with M and its value is ranged from 0 and L. Using (5) and (6), the even- and odd-mode input admittance can be rewritten as:

$$Y_{even} = \frac{j \cdot \omega C_2}{1 - \omega^2 (L_1 + M) C_2} \tag{7}$$

$$Y_{odd} = \frac{j \cdot \omega (2C_1 + C_2)}{1 - \omega^2 (L_1 - M)(2C_1 + C_2)} + j \cdot 2\omega C_1 \tag{8}$$

The resonances occur when the input admittance of the even- and odd-mode circuit approaches infinity. Solving $Y_{even} = \infty$ and $Y_{odd} = \infty$, it is possible to find the locations of two resonant frequencies of the resonator:

$$f_1 = \frac{1}{2\pi\sqrt{(L_1 - M)\cdot(2C_1 + C_2)}} \tag{9}$$

$$f_2 = \frac{1}{2\pi\sqrt{(L_1 + M)\cdot C_2}} \tag{10}$$

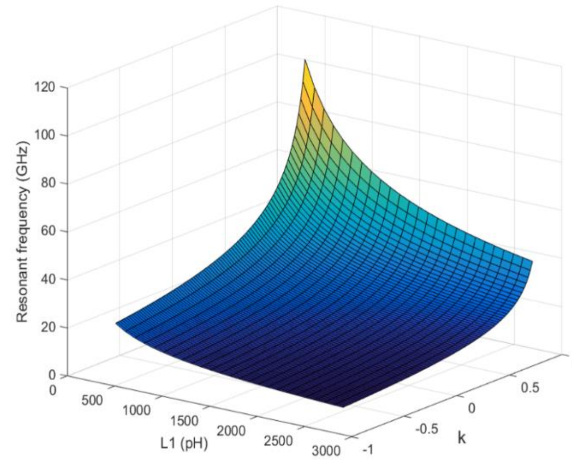

Fig. 9. 3D mapping of resonant frequency f_1 against k and L_1.

When the resonator is directly connected with I/O ports, the resonator will perform a filtering characteristic. Using the expressions of the even- and odd-mode input admittance, it is possible to calculate the scattering parameters (*S*-parameters) of the filter, which can be expressed as [27]:

$$S_{21} = \frac{Y_o(Y_{odd} - Y_{even})}{(Y_o + Y_{odd})(Y_o + Y_{even})}$$
$$S_{11} = \frac{Y_o^2 - Y_{even}Y_{odd}}{(Y_o + Y_{odd})(Y_o + Y_{even})} \tag{11}$$

Two different circuits with inverting- and non-inverting-coupled resonators are calculated and compared. Fig. 6 depicts the *S*-paramters of two BPFs based on these two different resonators, respectively. It is seen that when the coupling coefficients are the same in magnitude (k equals to -0.8 for inverting coupling and 0.8 non-inverting coupling) with opposite signs, the *S*-paraemters are totally different. This is because different types of coupling result in different resonant frequencies and transmission zeros of the filtering responses. To find out the intrisinc machnism, it is important to investigate the resonant modes and transmission zeros that are produced by the resonators.

C. Resonant Modes of the Resonators

As observed from Fig. 6, the resonance of the inverting-coupled structure occurs at about 14 GHz, while the resonance of the non-inverting-coupld one is at around 45 GHz, which is almost three times higher than the inverting-coupled case. This can be explained by (9) and (10). For the non-inverting-coupled case, the mutual inductance M is positive, and two resonant frequenies are written as f_{1_n} and f_{2_n}; on the other hand, for the case of inverting coupling, the mutual inductance M is negative, and two resonate frequencies are written as f_{1_i} and f_{2_i}. When the same amount of coupling inductance is considered in two cases, the resonant poles of f_{1_n}, f_{2_n}, f_{1_i} and f_{2_i} are located at different positions on the spectrum. As an example, when L_1 is selected as 1000 pH, C_1 = 20 fF and C_2 = 20 fF, the resonant mode distribution of the resonator is displayed in Fig. 7. When $0 < |k| < 0.5$, there is $f_{1\_i} < f_{1\_n} < f_{2\_n} <$

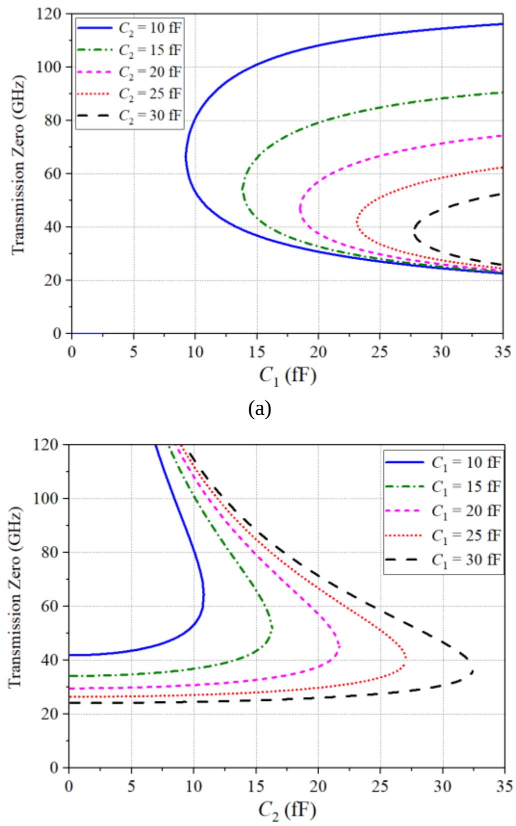

(a)

(b)

Fig. 10. The values of transmission zeros (a) varying against C_1 when C_2 is fixed; (b) varying against C_2 when C_1 is fixed.

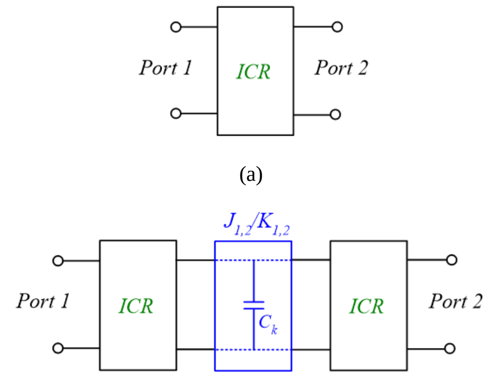

(a)

(b)

Fig. 11. Configuration of (a) a conventional 1st-order BPF; (b) a conventional 2nd-order BPF. Note: ICR stands for inverting-coupled resonator.

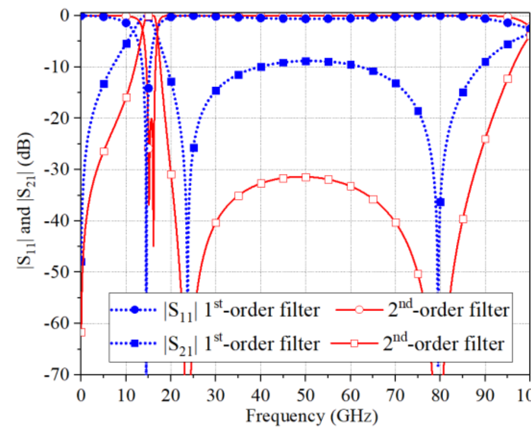

Fig. 12. S-parameters of the designed BPFs using inverting-coupled structure.

f_{2_i}; while when $0.5 < |k| < 1$, there is $f_{1\_i} < f_{2\_n} < f_{1\_n} < f_{2\_i}$. In both cases ($0 < |k| < 1$), it is found f_{1_i} is always located at the lowest frequency. The curves in Fig. 7 may vary when different values of C_1 and C_2 are chosen, but the relation of resonant poles is similar. This means that if the two resonators have same dimensions, the inverting-coupled one is likely to get its resonate pole located at the lower frequency. Besides, this phenomenon also explains why the calculated $|S_{21}|$ of the inverting-coupled case is located at a much lower frequency than the non-inverting coupled one, as is indicated in Fig. 6. It is obvious that the inverting-coupled one can produce a resonant pole at much lower frequency, which is favourable to be used in designing miniaturized BPF.

Fig. 8 shows the relation between k and f_1, f_2 with different values of C_1 and C_2. When $|k|$ is fixed, a smaller C_1 will result in a higher f_1, as seen from (9); on the other hand, the variance of C_1 does not affect f_2 because f_2 has nothing to do with C_1 as seen from (10). Similarly, a smaller C_2 will result in a higher f_1 and f_2, because C_2 contributes to the denominators of both f_1 and f_2 in (9) and (10). Since the capacitances of C_1 and C_2 are relatively small and constant (typically around 10-30 fF), the main affecting factor of the resonant poles to f_1 and f_2 are L_1 and k. Fig. 8 shows a 3-D mapping relation of resonant f_1 against L_1 and k. It is observed that a lower value of f_1 occurs at a larger value of L_1 and a larger value of $|k|$ when k is negative. In this design, the first resonant mode of the resonator f_1 under inverting coupled structure (as written as f_{1_i}) will be utilized as the resonant pole for design of BPFs in the following sections of this paper.

D. Transmission Zeros

Apart from the resonant modes, the inverting-coupled resonator can also generate multiple transmission zeros, which can be used to improve out-of-band suppression. The transmission zeros occur when the even-mode impedance and odd-mode impedance are equal to each other, which is $Y_{even} = Y_{odd}$. In this case, from (7) and (8) it is forced to have

$$\frac{j\cdot\omega C_2}{1-\omega^2(L_1+k\cdot L_1)C_2} = \frac{j\cdot\omega(2C_1+C_2)}{1-\omega^2(L_1-k\cdot L_1)(2C_1+C_2)} + j\cdot 2\omega C_1 \quad (12)$$

By solving (12), two solutions to ω can be derived, which correspond to the transmission zeros ω_{tz1} and ω_{tz2} that can be expressed as:

$$\omega_{tz1} = \sqrt{\frac{2C_1^2+2C_1C_2-2C_1^2k+C_2^2k+2C_1C_2k-\sqrt{P}}{2Q}} \quad (13)$$

$$\omega_{tz2} = \sqrt{\frac{2C_1^2+2C_1C_2-2C_1^2k+C_2^2k+2C_1C_2k+\sqrt{P}}{2Q}} \quad (14)$$

where

$$P = 4C_1^4k^2 - 8C_1^4k + 4C_1^4 + 8C_1^3C_2k^2 - 8C_1^3C_2 + 8C_1^2C_2^2k^2 + 12C_1^2C_2^2k - 4C_1^2C_2^2 + 4C_1C_2^3k^2 + 4C_1C_2^3k + C_2^4k^2$$

$$Q = -2L_1C_1^2C_2k^2 + 2L_1C_1^2C_2 - L_1C_1C_2^2k^2 + L_1C_1C_2^2$$

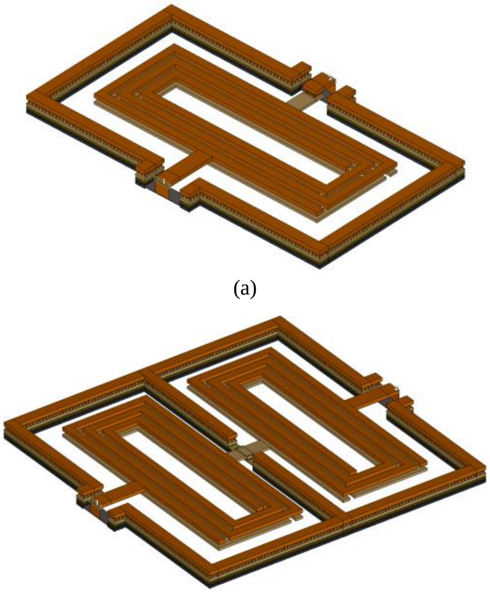

(a)

(b)

Fig. 13. 3-D views of the designed BPFs, (a) 1st-order one, (b) 2nd-order one.

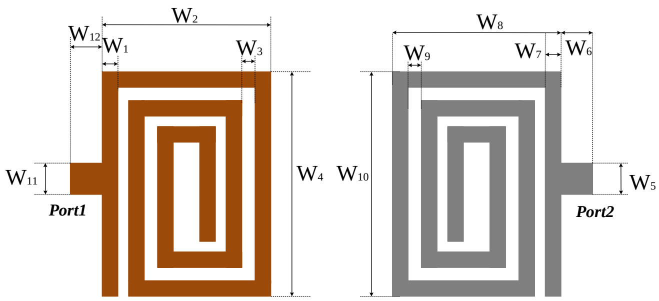

(a) (b)

Fig. 14. Layout of the 1st-order BPF: (a) upper layer spiral, and (b) lower layer spiral. Note: W_1 = 6 μm, W_2 = 74 μm, W_3 = 4 μm, W_4 = 190 μm, W_5 = 12 μm, W_6 = 12 μm, W_7 = 6 μm, W_8 = 74 μm, W_9 = 4 μm, W_{10} = 190 μm, W_{11} = 12 μm, and W_{12} = 12 μm.

The expressions of ω_{tz1} and ω_{tz2} are complicated and it is difficult to identify the effect of L_1, C_1 and C_2 on the zeros. However, by observing (13) and (14), one can find that L_1 is always on the denominators of ω_{tz1} and ω_{tz2}, which means the positions of transmission zeros are inversely proportional to L_1. Moreover, to investigate the effect of C_1 and C_2 on ω_{tz1} and ω_{tz2}, multiple cases with different values of C_1 and C_2 against the locations of transmission zeros, f_{tz1} and f_{tz2}, (which are equal to ω_{tz1} and ω_{tz2} divided by 2π), are shown in Fig. 10. When C_2 is fixed and C_1 increases from 10 to 30 *fF*, two transmission zeros will move closer to each other. When C_1 is smaller than a certain value, two transmission zeros will merge and disappear. This means that under such circumstance, equation (12) has no solutions. On the other hand, when C_1 is fixed and C_2 increases from 10 to 30 *fF*, f_{tz1} will move to lower frequencies, while f_{tz2} will move further higher. When C_2 is higher than a certain value, f_{tz1} and f_{tz2} will disappear as well. Therefore, it is quite important to select appropriate values for C_1 and C_2 to guarantee the transmission zeros are existing at the upper-stopband during the procedure of BPF design.

III. Design of 1st-Order and 2nd-Order BPFs

A. 1st-Order BPF

The presented inverting-coupled resonator has been proved to be able to produce multiple resonances and transmission zeros due to the inductive coupling between two metal layers. The resonances and transmission zeros can be easily controlled. Therefore, this type of resonator is favoured for BPF designs. As one knows, if the resonator is directly taped with two feeds, as indicated in Fig. 11(a), it is possible to build a 1st-order filter. Since the resonator can provide a transmission zero at DC, this 1st-order filter is a bandpass type. Apparently, the external quality factor is fixed, which has been pre-determined by the dimensions of the resonator. The external quality factor can be expressed as:

$$Q_{ex} = \frac{2Y_o g_o g_1}{b_r} \tag{15}$$

$$b_r = \frac{\omega_o \cdot \partial \mathrm{Im}[Y_{even}(\omega_o) + Y_{odd}(\omega_o)]}{4 \cdot \partial\omega} \tag{16}$$

where g_o and g_1 are the basic element value of a conventional *n*-stage lowpass filter prototype, and b_r is the the susceptance slope parameter of the resonator [27]. Y_{even} and Y_{odd} can be calculated from (7) and (8). In addition, the fractional bandwidth (FBW) of the passband is also fixed, due to the relation between the FBW and Q_{ex}:

$$FBW = \frac{g_0 g_1}{Q_{ex}} = \frac{b_r Y_0}{J_{0,1}^2} \tag{17}$$

$$J_{0,1} = \sqrt{\frac{b_r Y_0}{Q_{ex}}} = \sqrt{\frac{b_r FBW Y_0}{g_0 g_1}} \tag{18}$$

where $J_{0,1}$ refers to the value of the admittance inverter at the input/output port. Since no extra feeding network is used in Fig. 11(a), $J_{0,1}$ is also a fixed value in this design. To adjust the in-band ripple and out-of-band performance, a higher-order filter needs to be developed.

B. 2nd-Order BPF

Fig. 11(b) shows the configuration of a 2nd-order BPF which is also based on the presented inverting-coupled resonator. This 2nd-order BPF is composed of two identical resonators (previously used for 1st-order BPF implementation) and a shunted capacitor C_k in the middle, which acts like a J/K inverter to get the specified in-band coupling coefficient. The coupling coefficient can be expressed as:

$$k_{1,2} = \frac{FBW}{\sqrt{g_1 g_2}} = \frac{J_{1,2}}{b_r} \tag{19}$$

where

$$J_{1,2} = FBW\sqrt{\frac{b_r^2}{g_1 g_2}} \tag{20}$$

$J_{1,2}$ is the value of admittance inverter between two resonators, and it is realized by the shunted capacitor C_k. Therefore, the value of C_k can be found using the following formula:

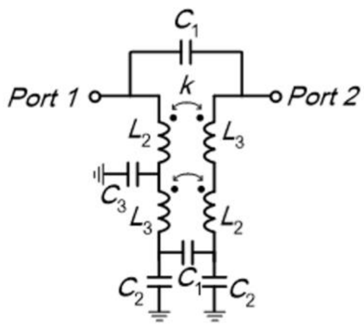

Fig. 15. Simplified *LC*-equivalent circuit of the modified inverting-coupled resonator.

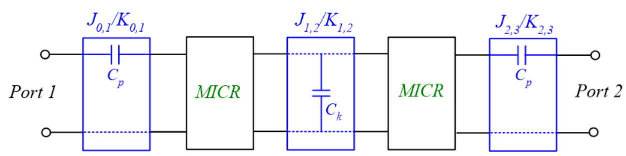

Fig. 16. Configuration of a 2nd-order BPF with controllable external *Q*-factor.

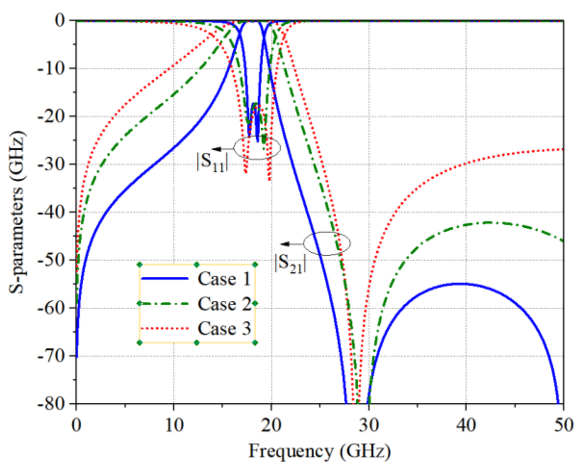

Fig. 17. S-parameters of three 2nd-order BPFs using MICR with different bandwidths.

$$C_k = \frac{J_{1,2}}{2\pi f_o} \tag{21}$$

As indicated in (12), to provide a suitable coupling between two resonators, the value of C_k should be determined according to $J_{1,2}$, which should be found based on the selection of FBW and b_r.

The S-parameters of the 1st- and 2nd-order BPFs are plotted in Fig. 12. Both of them have the same resonant poles and transmission zeros, which is because the same resonator is used. However, compared with the 1st-order BPF, the 2nd-order one has one more pole within the passband. Consequently, it provides a sharper selectivity and a better out-of-band performance. The 2nd-order BPF also has a more constant and flat in-band ripple compared with the 1st-order one. Although a good filtering response is achieved, the 2nd-order BPF also has a fixed bandwidth, which is a major drawback and should be improved. Finally, the 3-D view of the 1st- and 2nd-order BPFs is given in Fig. 13 and the physical dimensions used for electromagnetic (EM) simulation are summarized in Fig. 14.

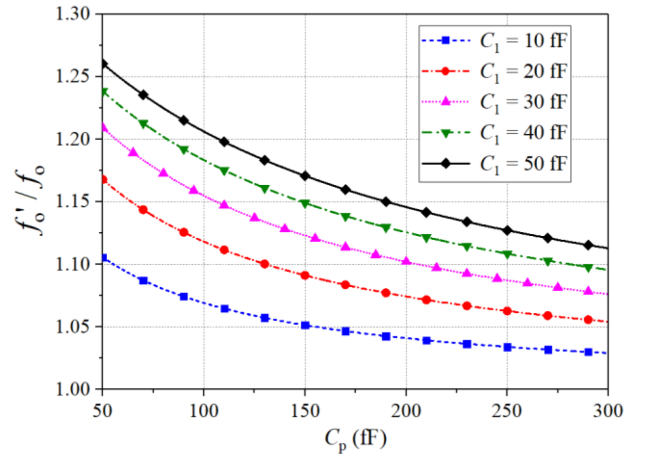

Fig. 18. The frequency ratio of f'_o/f_o against C_p when C_1 varies from 10 fF to 50 fF.

IV. Design of Modified 2nd-Order BPF with Bandwidth Control and Improved Upper-Stopband Suppression

A. Modified Inverting-Coupled Resonator

In Section III, a 2nd-order filter is designed based on two inverting-coupled resonators. By controlling the equivalent inductance of metal lines and the inter-stage capacitance between them, it is possible to allocate the resonance at the bandpass frequency and the harmonic resonance at the upper stopband. Meanwhile, two transmission zeros are generated which helps to enhance the passband selectivity and stopband suppression. Based on the existing design, a modified resonator which is called modified inverting-coupled resonator is proposed here, as shown in Fig. 15. Compared with the previously presented resonator, this one has an extra shunted capacitor C_3, which is located at one of the metal lines of the resonator, splitting L_1 into two parts, L_2 and L_3. When C_3 is in the middle point of the metal line, there is $L_2 = L_3 = L_1/2$. In this case, two spiral inductors become asymmetric, which would contribute to an additional transmission zero in the upper stopband of the filter.

B. Modified 2nd-Order BPF with Controllable Bandwidth

Based on the modified resonator, an improved 2nd-order BPF is built using the topology shown in Fig. 16. Compared with the initial 2nd-order BPF in Fig. 11(b), the modified design includes two cascaded capacitors C_p at the input/output feeds. The cascaded C_p plays the role of a J/K inverter, which can control the external quality factor and *FBW*. The bandwidth of the filter *FBW* can be expressed as:

$$FBW = \frac{(J_{01}^2/Y_o)g_0 g_1}{\omega_o \cdot \frac{\partial \mathrm{Im}[Y_{even}(\omega_o) + Y_{odd}(\omega_o)]}{4 \cdot \partial\omega}} \tag{22}$$

Therefore, to get a certain value of FBW, the required value of the admittance inverter $J_{0,1}$ and the capacitance C_p at the input/output port can be found to be:

$$J_{0,1} = \sqrt{\frac{\omega_o \cdot FBW \cdot Y_o \cdot \partial Im[Y_{even}(\omega_o) + Y_{odd}(\omega_o)]}{4 \cdot g_0 g_1 \cdot \partial\omega}} \tag{23}$$

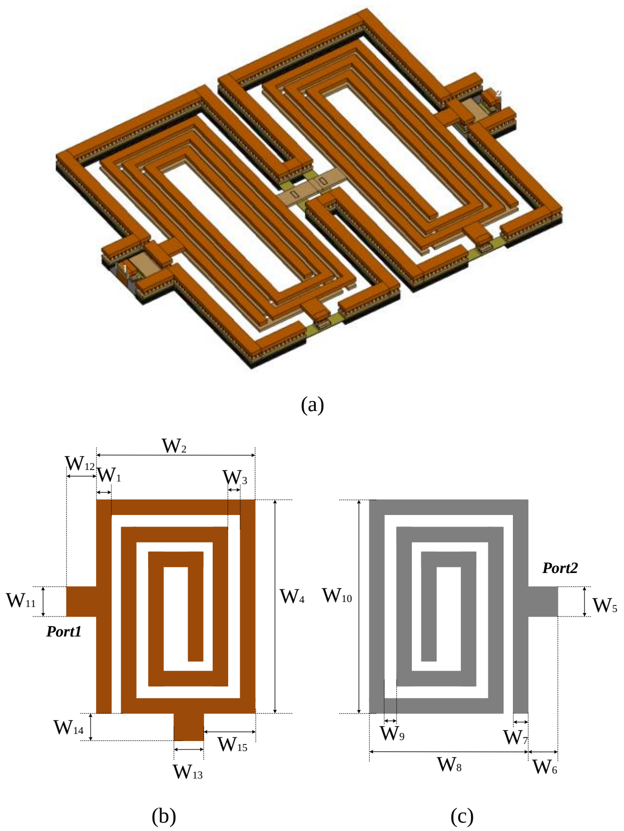

Fig. 19. Layout of the modified 2nd-order BPF: (a) 3-D view of the modified 2nd-order BPF, (b) upper spiral layer; and (c) lower spiral layer. Note: W_1 = 6 μm, W_2 = 74 μm, W_3 = 4 μm, W_4 = 180 μm, W_5 = 12 μm, W_6 = 12 μm, W_7 = 6 μm, W_8 = 74 μm, W_9 = 4 μm, W_{10} = 180 μm, W_{11} = 12 μm, W_{12} = 12 μm, W_{13} = 12 μm and W_{14} = 12 μm.

$$C_p = \frac{J_{0,1}}{2\pi f_o \sqrt{1-\left(J_{0,1}/Y_o\right)^2}} \tag{24}$$

When the resonator is fixed, the susceptance slope parameter b_r is also fixed. Thus, the FBW is inverse proportional to $J_{0,1}^2$, which means a smaller value of $J_{0,1}$ will result in a larger bandwidth of the BPF. Based on this relation, the bandwidth of the passband can be simply controlled by changing the value of C_p, which is closely related to $J_{0,1}$. Fig. 17 shows the S- parameters of three cases with different FBW, while the same resonator is used. It is clearly seen that three bandpass filtering responses are realized with exactly the same center frequency and transmission zero, but different bandwidth. When C_p is varied from 5 fF to 100 fF, the FBW can be tuned from 10% to 30%. Meanwhile, by slightly adjusting the value of C_k, one can make the in-band ripple at an optimal level.

C. Frequency Shift in the Modified 2nd-Order BPF

Due to the existence of C_p, the resonant frequency will shift to a higher frequency. This is because C_p also contributes to a part of the resonator in the modified 2nd-order bandpass filter. To investigate the frequency shift range, the equivalent even- and odd-mode admittance including the effect of C_p should be modified as:

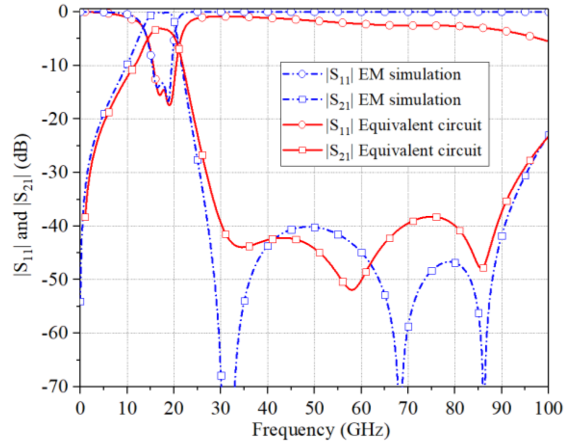

Fig. 20. Comparisons between the S-parameters of the modified 2nd-order BPF obtained from EM simulation and simplified circuit model.

$$Y'_{even} = \frac{j\omega C_p \cdot Y_{even}}{j\omega C_p + Y_{even}} \tag{25}$$

$$Y'_{odd} = \frac{j\omega C_p \cdot Y_{odd}}{j\omega C_p + Y_{odd}} \tag{26}$$

Since the resonance in the passband occurs under the conditions of $Y'_{odd} = \infty$, the resonant frequency with the effect of C_p can be calculated as:

$$f'_o = \frac{1}{2\pi}\sqrt{\frac{4C_1+C_2+C_p}{(2C_1+C_p)\cdot(L_1-M)\cdot(2C_1+C_2)}} \tag{27}$$

Compared with the original resonant frequency f_o given in (9), the resonant frequency f'_o in the modified 2nd-order BPF has a factor of q, where

$$q = \sqrt{\frac{4C_1+C_2+C_p}{2C_1+C_p}} \tag{28}$$

In other words, $f'_o = f_o \cdot q$. It is obvious that $q > 1$, which means the original resonant frequency will definitely move to a higher frequency due to the existence of C_p. Since the value of C_p is much larger than C_1 and C_2, the value of q is just a little bit larger than 1. Fig. 18 shows the relation between the ratio of f'_o/f_o against C_p when C_1 varies from 10 fF to 50 fF. It is clearly seen that the ratio of f'_o/f_o moves towards 1 when C_p increases, and a larger C_1 will lead to a more frequency shift of f'_o from f_o. This frequency shift can be compensated by slightly tuning the parameters of the BPF, such as L_1 and C_k, to adjust the resonant frequency and coupling coefficient back to the original status.

Fig. 19 shows the 3-D view as well as the layout of the modified 2nd-order BPF. Moreover, to prove that the presented simplified *LC*-equivalent circuit model is sufficiently accurate for predicting the characteristic of the design, EM simulated results are compared with those from the circuit model, which are shown in Fig. 19. The following values are chosen for the relevant parameters in the equivalent circuit: L_2 = 450 pH, L_3 = 100 pH, C_1 = 35 fF, C_2 = 25 fF, C_p = 250 fF, C_k = 100 fF, and k = -0.9. It is clearly seen that three transmission zeros are located at the upper-stopband of the filter, which greatly improves the harmonic suppression capability of the filter.

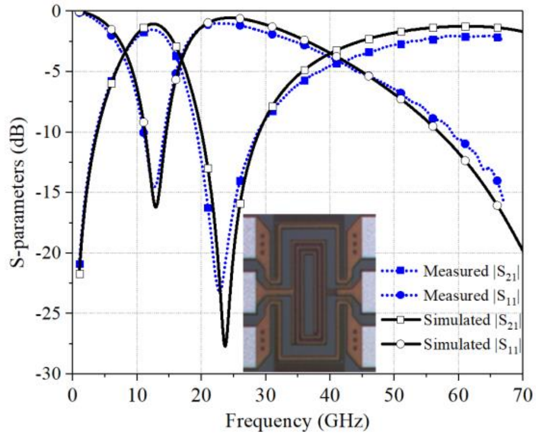

(a)

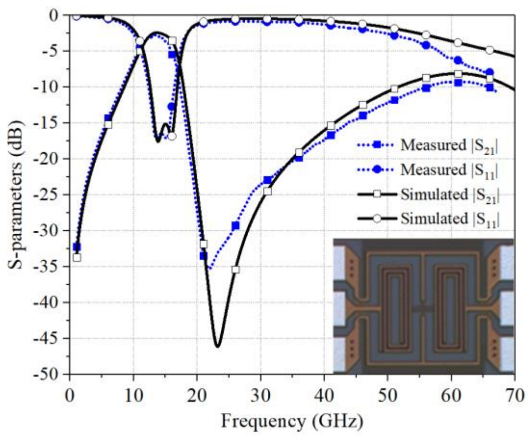

(b)

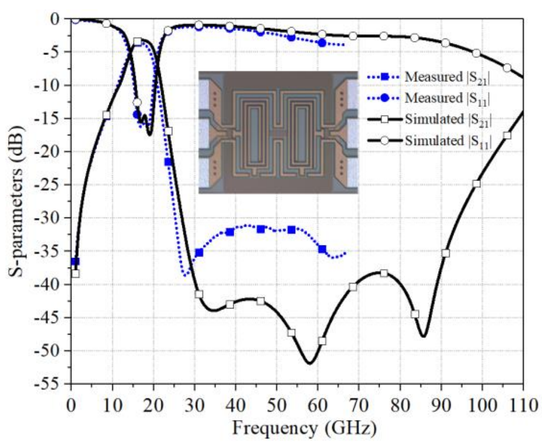

(c)

Fig. 21. Measured S-parameters of all three designs, (a) 1st-order BPF, (b) 2nd-order BPF, (c) modified 2nd-order BPF with improved out-of-band suppression.

V. Measurement Results and Discussions

A. On-Wafer Measurement Results

To fully evaluate the performance of the above presented designs, all three BPFs are fabricated in a standard 0.13-µm (Bi)-CMOS technology. The die microphotographs are embedded with the measured results, which are given in Fig. 20. Excluding the pads, their physical dimensions are 0.13 × 0.25 mm^2, 0.26 × 0.25 mm^2, 0.24 × 0.22 mm^2, respectively. Using a vector network analyser (VNA), ME7838A, from Anritsu, all circuits are measured via on-wafer G-S-G probing, from 1 GHz up to 67 GHz. Measurements were made by using conventional open-short-load-through (OSLT) on-wafer calibration to move the reference planes from the connectors of the equipment to the tips of the RF probes. For comparison, both the simulated and measured $|S_{21}|$ and $|S_{11}|$ (also known as return loss) of all the three designs are plotted in each figure.

For the 1st-order BPF, the results are shown in Fig. 21(a). As can be seen, it has a center frequency at 12.5 GHz with a bandwidth of 24%. The minimum insertion loss is 1.5 dB, while the maximum out-of-band suppression of 23.3 dB is obtained at 23 GHz. The results of the 2nd-order BPF that simply cascades two 1st-order BPF with some additional inter-stage capacitors are presented in Fig. 21(b). It has a centre frequency of 14 GHz with a 28.6% bandwidth. The minimum insertion loss and maximum out-of-band suppression are 2.5 dB and 35 dB, respectively. Finally, the results for the modified 2nd-order BPF are given in Fig. 21(c). As can be seen, this design has a center frequency at 17 GHz with a bandwidth of 27.8%. In addition, the minimum insertion loss is 3.5 dB and the out-of-band suppression is better than 30 dB from 25 to 67 GHz (limited by equipment).

All in all, fairly reasonable agreements between the EM simulated and the measured results for all three designs have been achieved. The discrepancy between them and some ripples appeared in the tested results below 20 dB are likely to be caused by the G-S-G pads and testing environment, which are not included in EM simulation.

B. Discussions

To demonstrate the performance improvement of the presented design over other state-of-the-art ones, a comparison table is given in Table I. Depending on different design specifications, a BPF can be designed with flexibility to satisfy different requirements using the concept presented in this work. Comparing the Design 1 and 2 with other works, they have achieved the lowest insertion loss with miniaturized physical dimensions. Although the insertion loss of the Design 3 is slightly higher than the average one, it has successfully demonstrated a superior out-of-band suppression to the 4th-order harmonic frequency at least.

It is noted that some parasitic capacitance from another side of the inductor to the ground is not considered in the equivalent circuit, because it is fairly small comparing with other parasitic capacitance, and thus it only has marginal impact on frequency responses of BPF design. For example, if the parasitic capacitors at Ports 1 and 2 are added in the equivalent circuit, the frequency responses of the BPF will not change much, in terms of the bandwidth, center frequency, positions of transmission zeros, in-band ripple and stopband level. Therefore, the parasitic capacitance is neglected in the synthesis for simplicity. Moreover, although the methodology in this work is only demonstrated for BPFs design around 15 GHz, the method can be directly transferred to higher operation frequencies as well. There is no fundamental limitation for

TABLE I
PERFORMANCE SUMMARY OF THE DESIGNED BPFS WITH OTHER STATE-OF-THE-ART DESIGNS

REF.	*fc* (GHz)	Insertion loss (dB)	Filter order	Fractional bandwidth (%) ^	No. of TZs	Stopband bandwidth @ more than 30 dB suppression (GHz)	Stopband suppression @ high frequency (dB)	Area (mm^2)	Tech. (µm)
[3]	60	9.3	1st	10	n/a	n/a	n/a	0.11	0.18 CMOS
[5]	25	2.5	2nd	31	3	51-70	38	0.28	0.13 CMOS
[12]	65	3.4	2nd	18.5	2	n/a	30	0.074	0.18 CMOS
[17]	60	2.5	1st	21	2	n/a	20	0.156	0.18 CMOS
[18]	59.5	3.3	2nd	21.7	2	n/a	27	0.054	0.18 CMOS
[20]	35	4.5	2nd	37.8	**2**	56-85	50	0.124	0.18 CMOS
[21]	33	2.6	2nd	42.4	n/a	72-110	n/a	0.03	0.13 SiGe
[22]	35	3.1	3rd	50	3	55-62	35	0.075	0.13 SiGe
[23]	40	1.7	1st	20	1	n/a	21	0.012	0.13 SiGe
[24]	31	2.4	1st	22.6	1	n/a	20	0.024	0.13 SiGe
[25]	33	2.6	1st	18	**1**	58-70	44	0.031	0.13 SiGe
DESIGN 1	**12.5**	**1.5**	**1st**	**24**	**2**	**n/a**	**23**	**0.033**	**0.13 SiGe**
DESIGN 2	**14**	**2.5**	**2nd**	**28.6**	**2**	**20-26**	**35**	**0.065**	**0.13 SiGe**
DESIGN 3	**17**	**3.5**	**2nd**	**27.8**	**3**	**25-67**	**38**	**0.053**	**0.13 SiGe**

using this method to implement a BPF at a higher frequency, such as 30 or 60 GHz. A relatively lower frequency is chosen due to the fact that the motivation behind this work is miniaturization. When operation frequency of passive devices is pushing up to millimeter-wave region, their physical dimensions are inherently shrinking. Thus, the miniaturization of devices becomes less critical. Moreover, due to the limitation of the measurement systems, the S-parameters can only be measured up to 67 GHz, which means if the BPFs were designed at higher frequencies, it would be quite difficult to measure the frequency responses at the upper-stopband range, especially to investigate the suppression capability of the 2nd- and 3rd-order harmonics.

VI. CONCLUSIONS

In this work, two different coupling structures, namely inverting coupling and non-inverting coupling, are analysed and compared. The possibility of using them for miniaturized BPFs design is investigated. To fully understand the insight of these structures as well as effectively use them for BPFs design, simplified *LC*-equivalent circuit models are developed. Using the models, three BPFs are designed and implemented. To further prove that the presented approach is feasible in practice, all designs are fabricated in a standard 0.13-µm (Bi)-CMOS technology. The sizes of them without pads are very small. A reasonable agreement between the EM simulated and measured results for all designs is obtained. According to the overall performances of the designed BPFs, it can be concluded that this approach is particularly suitable for miniaturized RFIC design in silicon-based technologies.

REFERENCES

[1] K. Y. Wu, X. Ding, M. Ismail and H. Olsson, "RF bandpass filter design based on CMOS active inductors," *IEEE Trans. Circuits Syst. II*, vol. 50, no. 12, pp. 942–949, Dec. 2003.

[2] G. Leuzzi, V. Stornelli, S. D. Re, "A Tuneable Active Inductor With High Dynamic Range for Band-Pass Filter Applications," *IEEE Trans. Circuits Syst. II*, vol. 58, no. 10, pp. 647-651, 2011.

[3] L. Nan, K. Mouthaan, Y. Z. Xiong, J. Shi, S. C. Rustagi, and B. L. Ooi, "Design of 60- and 77-GHz narrow-bandpass filters in CMOS technology," *IEEE Trans. Circuits Syst. II, Exp. Briefs*, vol. 55, no. 8, pp. 738-742, Aug. 2008.

[4] J. R. Long, Y. Zhao, W. Wu, M. Spirito, L. Vera, and E. Gordon, "Passive circuit technologies for mm-wave wireless systems on silicon," *IEEE Trans. Circuits Syst. I, Reg. Papers*, vol. 59, no. 8, pp. 1680-1693, Aug. 2012.

[5] C. –L. Yang, S. –Y. Shu, and Y. –C. Chiang, "Design of a K-band chip filter with three tunable transmission zeros using a standard 0.13-µm CMOS technology," *IEEE Trans. Circuits Syst. II, Exp. Briefs*, vol. 57, no. 7, pp. 522–526, Jul. 2010.

[6] R. Shu, J. Li, T. Adrian, B. J. Drouin, and Q. J. Gu, "Coupling-inductor based hybrid mm-wave CMOS SPST switch," *IEEE Trans. Circuits Syst. II, Exp. Briefs*, vol. 64, no. 4, pp. 367-371, Apr. 2017.

[7] Z. J. Hou et al., "A W-band balanced power amplifier using broadside coupled strip-line coupler in SiGe Bi-CMOS 0.13-µm technology," *IEEE Trans. Circuits Syst. I, Reg. Papers*, vol. 65, no. 7, pp. 2139-2150, Jul. 2018.

[8] H. Chung, Q. Ma and G. M. Rebeiz, "A 10-40 GHz frequency quadrupler source with switchable bandpass filters and > 30 dBc harmonic rejection," *IEEE Radio Frequency Integrated Circuits Symposium (RFIC)*, pp. 49-52. Honolulu, HI, 2017.

[9] S. Sun, J. Shi, L. Zhu, S. C. Rustagi, and K. Mouthaan, "Millimeter-wave bandpass filters by standard 0.18-µm CMOS technology," *IEEE Electron Device Lett.*, vol. 28, no. 3, pp. 220-222, Mar. 2007.

[10] W. Z. Chen, W. H. Chen, and K. C. Hsu, "Three-dimensional fully symmetric inductors, transformer, and balun in CMOS technology," *IEEE Trans. Circuits Syst. I, Reg. Papers*, vol. 54, no. 7, pp. 1413–1423, Jul. 2007.

[11] M. K. Chirala, X. Guan and C. Nguyen, "Integrated multilayered on-chip inductors for compact CMOS RFICs and their use in a miniature distributed low-noise-amplifier design for ultra-wideband applications," *IEEE Trans. Microw. Theory Tech*., vol. 56, no. 8, pp. 1783-1789, Aug. 2008.

[12] S. -C. Chang, Y. -M. Chen, S. -F. Chang, Y. -H. Jeng, C. -L. Wei, C. -H. Huang and C. -P. Jeng, "Compact millimeter-wave CMOS bandpass filters using grounded pedestal stepped-impedance technique," *IEEE Trans. Microw. Theory Tech.*, vol. 58, no. 12, pp. 3850-3859, Dec. 2010.

[13] Y. -S. Lin and V. K. Nguyen, "94-GHz CMOS power amplifiers using miniature dual Y-shaped combiner with RL load," *IEEE Trans. Circuits Syst. I, Reg. Papers*, vol. 64, no. 6, pp. 1285–1298, Jun. 2017.

[14] I. C. H. Lai, Y. Kambayashi and M. Fujishima, "60-GHz CMOS down-conversion mixer with slow-wave matching transmission lines," *Proc. IEEE Asian Solid-State Circuits Conf.*, pp. 195-198, Nov. 2006.

[15] A.-L. Franc, E. Pistono, G. Meunier, D. Gloria, P. Ferrari, "A lossy circuit model based on physical interpretation for integrated shielded slow-wave CMOS coplanar waveguide structures," *IEEE Trans. Microw. Theory Techn.*, vol. 61, no. 2, pp. 754-763, Feb. 2013.

[16] K. Kim and C. Nguyen, “An ultra-wideband low-loss millimeter-wave slow-wave Wilkinson power divider on 0.18-μm SiGe Bi-CMOS process,” *IEEE Microw. Wireless Componen. Lett.*, vol. 25, no. 5, pp. 331-333, May 2015.
[17] N. Mahmoud, A. Barakat, A. B. Abdel-Rahman, A. Allam, R. K. Pokharel, “Compact size on-chip 60 GHz H-shaped resonator BPF,” *IEEE Microw. Wireless Compon. Lett*., vol. 26, no. 9, pp. 681-683, Sep. 2016.
[18] A. S. A. EI-Hameed, A. Barakat, A. B. Abdel-Rahman, A. Allam, R. K. Pokharel, “Ultra compact 60-GHz CMOS BPF employing broadsided-coupled open-loop resonators,” *IEEE Microw. Wireless Compon. Lett.*, vol. 27, no. 9, pp. 818-820, Sep. 2017.
[19] P. Sarafis, A. G. Nassiopoulou, H. Issa, and P. Ferrari, “High performance on-chip low-pass filters using CPW and slow-wave-CPW transmission lines on porous silicon,” *IEEE Trans. Electron Devices*, vol. 63, no. 1, pp. 439–445, Jan. 2016.
[20] L. -K. Yeh, C. -Y. Chen and H. -R. Chuang, “A millimeter-wave CPW CMOS on-chip bandpass filter using conductor-backed resonators,” *IEEE Electron Devices Lett.*, vol. 31, no. 5, pp. 399-401, May 2010.
[21] Y. Yang, H. Liu, Z. J. Hou, X. Zhu, E. Dutkiewicz, and Q. Xue, “Compact on-chip bandpass filter with improved in-band flatness and stopband attenuation in 0.13-μm (Bi)-CMOS technology,” *IEEE Electron Device Lett.*, vol. 38, no. 10, pp. 1359-1362, Oct. 2017.
[22] H. Zhu, X. Zhu, Y. Yang and Q. Xue, “Design of wideband third-order bandpass filters using broadside-coupled resonators in 0.13-μm (Bi)-CMOS technology,” *IEEE Trans. Microw. Theory Techn. Early Access*.
[23] H. Zhu, Y. Yang, X. Zhu, Y. Sun, and S. W. Wong, “Miniaturized resonator and bandpass filter for silicon-based monolithic microwave and millimeter-wave integrated circuits,” *IEEE Trans. Circuits Syst. I, Reg. Papers*, vol. 65, no. 12, pp. 4062–4071, Dec. 2018.
[24] S. Chakraborty, *et al*., “A broadside-coupled meander-line resonator in 0.13-μm SiGe technology for millimeter-wave application,” *IEEE Electron Devices Lett.*, vol. 37, no. 3, pp. 329-331, Mar. 2016.
[25] Y. Zhong, Y. Yang, X. Zhu, E. Dutkiewicz, K. M. Shum and Q. Xue, “An on-chip bandpass filter using a broadside-coupled meander line resonator with a defected-grounded structure,” *IEEE Electron. Device Lett.*, vol. 38, no. 5, pp. 626-629, May. 2017.
[26] Y. Yang, X. Zhu, E. Dutkiewicz, and Q. Xue, “Design of a miniaturized on-chip bandpass filter using edge-coupled resonators for millimeter-wave applications,” *IEEE Trans. Electron Devices*, vol. 64, no. 9, pp. 3822-3828, Sep. 2017.
[27] J. S. Hong and M. J. Lancaster, *Microstrip Filter for RF/Microwave Applications*. Hoboken, NJ, USA: Wiley, 2001.

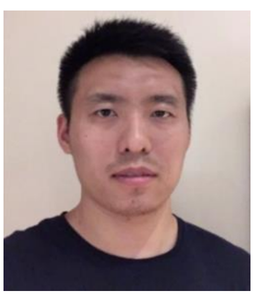

He Zhu (M’18) received the bachelor’s degree and master’s degrees from South China University of Technology (SCUT), Guangzhou, China, in 2011 and 2014, and the Ph.D. degree from School of Information Technology and Electrical Engineering (ITEE), The University of Queensland, Brisbane, Australia, in 2017.

He is currently a Post-doctoral Research Fellow with Global Big Data Technologies Centre (GBDTC), University of Technology Sydney, Ultimo, NSW, Australia. His research interests include the development of tunable microwave and mm-wave devices, radio frequency integrated circuits and systems, and beam-forming networks for antenna arrays.

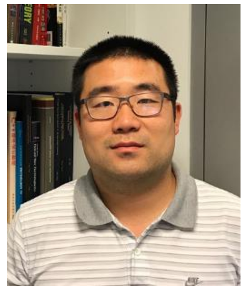

Xi Zhu (M’18) received the B.E. (Hons.) and PhD from University of Hertfordshire (UH), Hertfordshire, UK, in 2005 and 2008, respectively. He is currently a Lecturer with the School of Electrical and Data Engineering, Faculty of Engineering & IT, University of Technology Sydney, NSW, Australia. His research activities mainly involve in the areas of analogue baseband, radio frequency (RF) and mm-wave circuits and systems design. He has co-authored over 80 refereed publications in the above-mentioned fields.

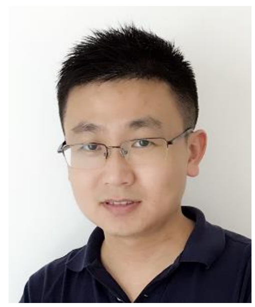

Yang Yang (S’11–M’14-SM’17) was born in Bayan Nur, Inner Mongolia, China and received the PhD degree from Monash University, Melbourne, Australia, in 2013.

From July 2012 to April 2015, he was an Asia Pacific GSP Engineer at Rain Bird and a Global GSP Success Award holder of the year 2014. From April 2015 to April 2016, he served as a Senior Research Associate with Department of Engineering, Macquarie University, Sydney, Australia. From April 2016 to December 2016, he was a Research Fellow with State Key Laboratory of Millimeter-Waves, City University of Hong Kong. Dr. Yang is currently a Senior Lecturer of University of Technology Sydney, Australia. His research interests focus on millimeter-wave circuits and antennas for 5G and beyond, and wearable medical sensing devices. He is a current Associate Editor of IEEE ACCESS and a current Area Editor of MICROWAVE OPTICAL TECHNOLOGY LETTERS.

Dr Yang is a winner of CST University Publication Award 2018, by CST, Germany.

Yichuang Sun (M’90-SM’99) received the B.Sc. and M.Sc. degrees from Dalian Maritime University, Dalian, China, in 1982 and 1985, respectively, and the Ph.D. degree from the University of York, York, U.K., in 1996, all in communications and electronics engineering.

Dr. Sun is currently Professor of Communications and Electronics, Head of Communications and Intelligent Systems Research Group, and Head of Electronic, Communication and Electrical Engineering Division in the School of Engineering and Computer Science of the University of Hertfordshire, UK. He has published over 330 papers and contributed 10 chapters in edited books. He has also published four text and research books: Continuous-Time Active Filter Design (CRC Press, USA, 1999), Design of High Frequency

Integrated Analogue Filters (IEE Press, UK, 2002), Wireless Communication Circuits and Systems (IET Press, 2004), and Test and Diagnosis of Analogue, Mixed-signal and RF Integrated Circuits - the Systems on Chip Approach (IET Press, 2008). His research interests are in the areas of wireless and mobile communications, RF and analogue circuits, microelectronic devices and systems, and machine learning and deep learning.

Professor Sun was a Series Editor of IEE Circuits, Devices and Systems Book Series (2003-2008). He has been Associate Editor of IEEE Transactions on Circuits and Systems I: Regular Papers (2010-2011, 2016-2017, 2018-2019). He is also Editor of ETRI Journal, Journal of Semiconductors, and Journal of Sensor and Actuator Networks. He was Guest Editor of eight IEEE and IEE/IET journal special issues: High-frequency Integrated Analogue Filters in IEE Proc. Circuits, Devices and Systems (2000), RF Circuits and Systems for Wireless Communications in IEE Proc. Circuits, Devices and Systems (2002), Analogue and Mixed-Signal Test for Systems on Chip in IEE Proc. Circuits, Devices and Systems (2004), MIMO Wireless and Mobile Communications in IEE Proc. Communications (2006), Advanced Signal Processing for Wireless and Mobile Communications in IET Signal Processing (2009), Cooperative Wireless and Mobile Communications in IET Communications (2013), Software-Defined Radio Transceivers and Circuits for 5G Wireless Communications in IEEE Transactions on Circuits and Systems-II (2016), and the 2016 IEEE International Symposium on Circuits and Systems in IEEE Transactions on Circuits and Systems-I (2016). He has also been widely involved in various IEEE technical committee and international conference activities.